Journal of Applied Physics

Multi-scale dynamics of atmospheric-pressure discharges ignited over liquid electrodes

Cite as: J. Appl. Phys. **127**, 043301 (2020); https://doi.org/10.1063/1.5132319
Submitted: 17 October 2019 . Accepted: 22 December 2019 . Published Online: 22 January 2020

Dmitry Levko, Robert R. Arslanbekov, and Vladimir I. Kolobov

Journal of Applied Physics ARTICLE scitation.org/journal/jap

Multi-scale dynamics of atmospheric-pressure discharges ignited over liquid electrodes

Cite as: J. Appl. Phys. **127**, 043301 (2020); doi: 10.1063/1.5132319
Submitted: 17 October 2019 · Accepted: 22 December 2019 ·
Published Online: 22 January 2020

Dmitry Levko,[1,a)] Robert R. Arslanbekov,[1] and Vladimir I. Kolobov[1,2]

AFFILIATIONS

[1]CFD Research Corporation, 701 McMillian Way, Huntsville, Alabama 35806, USA
[2]Center for Space Plasma and Aeronomic Research, University of Alabama in Huntsville, Huntsville, Alabama 35899, USA

[a)]**Author to whom correspondence should be addressed:** dima.levko@cfdrc.com

ABSTRACT

A multiphase computational model of atmospheric-pressure gas discharges ignited over liquid electrodes is developed. The model takes into account both the liquid electrode motion under applied electric fields and plasma generation in the gas phase. The influence of the applied voltage and liquid properties (density, viscosity, and surface tension) on the liquid surface deformation is analyzed. It is shown that the shape of dynamic cones formed on the liquid surface differs from the static Taylor's cones. The influence of the liquid surface protrusions on gas breakdown dynamics is demonstrated. It is shown that the breakdown develops in two stages: first, a fast ionization wave propagates from the cathode to the anode, and then the cathode sheath collapses due to secondary electron emission from the liquid surface. It is shown that dynamics of the multiphase system containing gas, plasma, and liquid states is characterized by three disparate time scales: the fast electron time scale, the intermediate ion time scale, and the slow liquid dynamics time scale.

I. INTRODUCTION

Plasma processes at gas-liquid interfaces have been studied for many decades.[1] Already in the first experimental studies,[1] it was observed that when an electric current from gas plasma flowed into a conducting liquid, remarkable chemical reactions occurred in the liquid phase. This process was referred to as a glow-discharge electrolysis.[1–3] It differs fundamentally from the conventional gas discharges since in the glow-discharge electrolysis, the liquid serves as one of the electrodes and the reactions of interest occur in the liquid phase.

Another method of generating plasma at gas-liquid interface was studied in Refs. 4–8 and reviewed in Refs. 9 and 10. In this method, dc voltage was applied between a pin metal electrode and a metal plate located under liquid surface. In was found that depending on the ratio between the pin radius (r) and the gap d between the liquid surface and the pin, there are three different discharge regimes:[9]

(1) At $r/d \geq 1$, gas breakdown is triggered by an instability of water surface in electric fields. Fast imaging showed that a Taylor cone[11] is formed on the liquid surface before the gas breakdown occurs. The liquid surface instability occurs when the electrostatic force cannot be compensated by gravity and surface tension.
(2) At $r/d \ll 1$, a stable corona discharge is formed near the pin before the gas breakdown occurred.[10] The ionic wind produced by the corona caused a depression of the liquid surface underneath the pin electrode.
(3) For the intermediate case, at $r/d \sim 1$, no stable corona discharge was formed and the breakdown occurred between the pin electrode and a static water surface.

The formation of electrically driven liquid jets from the tip of Taylor cones (without plasma formation) is of interest by itself for electrospraying.[12–14] The jets can be used, for instance, for high-resolution printing and for 2D material fabrication.[15] Insulating or conducting polymers can be printed with high resolution on planar or curved surfaces using this technique.[16] Fabrication of various devices like organic light-emitting diodes and biosensors that are further examples of electrohydrodynamic printing requires production of fine uniform drops with high precision control.[17,18] In addition, as was reported in Ref. 19, jets or microdroplets chemically activated by plasma can be used for food disinfection and cleaning of fresh produce.

In spite of countless experimental studies of gas plasma-in-contact with liquids (see reviews in Refs. 9 and 10 and references

therein), there are still no computational models, which consider both the liquid electrode dynamics and the gas plasma dynamics simultaneously. This is explained by several reasons. First, the problem is multidisciplinary and requires the knowledge of gas discharge physics and multiphase flow science.[10] Second, the problem is characterized by a wide range of time scales. We will show below that there are three vastly different intrinsic time scales associated with this problem: the slow liquid motion time scale (usually, milliseconds), the fast electron time scale (nanoseconds), and an intermediate ion time scale (microseconds). Most of the computational studies performed so far were focused on one side of the problem, either the liquid electrode dynamics[20,21] or the plasma-in-contact with "frozen" liquid electrode (see Refs. 22–24 and references therein). The shape of the liquid electrode was usually chosen from general physical considerations rather than a specific solution to the two-phase flow problem. Only recently, computational models of plasma in contact with liquid that consider mutual effects of plasma-liquid interactions have appeared in the press.[25] The model of Ref. 25 has studied effects of ion motion in collisionless sheath in front of a liquid cathode on liquid surface instability in electric fields with electrons assumed to be in equilibrium with the electric field.

In the present paper, we introduce a general approach to multiphase plasma treatment and identify the characteristic time scales, which can be used to justify approximations and to develop efficient computational models for such multiscale systems. In the present paper, we analyze dynamics of atmospheric-pressure discharges ignited over liquid electrodes. Our model takes into account both the liquid electrode motion due to electrohydrodynamic effects and plasma generation in the gas phase. We focus on the discharge ignition triggered by the protrusions formed on the liquid surface.

The paper is organized as follows. In Sec. II, we present details of our numerical model. In Sec. III, we analyze the liquid electrode dynamics in external electric fields. In Secs. IV and V, we analyze the gas breakdown dynamics. Results are summarized in the Conclusion section.

II. NUMERICAL MODEL

The computational model used in our studies was built on top of the open-source Basilisk framework designed for solving partial differential equations with adaptive Cartesian mesh.[26] The target application of the Basilisk code is multiphase flow science.

Due to the disparity of liquid and plasma time scales, we divided our model into two submodels. The first submodel considers only the liquid electrode dynamics. It solves the incompressible Navier-Stokes equations for two-phase gas-liquid flows,

$$\rho\frac{\partial \boldsymbol{u}}{\partial t}+\rho(\boldsymbol{u}\cdot\nabla)\boldsymbol{u}=\nabla\cdot[-p\boldsymbol{I}+\mu(\nabla\boldsymbol{u}+(\nabla\boldsymbol{u})^{T})]+\boldsymbol{F}, \quad (1)$$

$$\nabla\cdot\boldsymbol{u}=0. \quad (2)$$

Here, ρ is the mass density of the medium (either gas or liquid), μ is the medium viscosity, $\boldsymbol{u}$ is the velocity, p is the pressure, and $\boldsymbol{I}$ is the identity tensor. The term $\boldsymbol{F}$ on the right-hand side of Eq. (1) describes the force acting on the liquid only along the liquid-gas interface. This force consists of two components, namely, the surface tension and the electrostatic forces,[27]

$$\boldsymbol{F}=\left(\sigma\kappa-\frac{1}{2}\varepsilon_0 E^2\right)\delta_s\boldsymbol{n}. \quad (3)$$

The gas-liquid interface is tracked using the Volume-of-Fluid (VoF) method.[28] In this method, the interface is reconstructed from the fraction of each phase (gas and liquid) that exists within each computational cell; as a result, volume is conserved exactly. In Eq. (3), δ_s is the delta-function used in the VoF method, κ is the liquid curvature, E is the electric field at the liquid-gas interface, and $\boldsymbol{n}$ is the vector normal to the liquid surface.

Figure 1 shows the typical geometry used in our studies. The computational domain is the square box 5×5 mm. The domain consists of the gas phase (yellow color) and the liquid phase (blue color). The anode (top boundary) is grounded, while the negative constant potential φ_C is applied to the bottom boundary (cathode). The liquid considered in the present studies is water. The dimensions and initial shape of the liquid surface were taken to reflect the experiments in Ref. 8, where the liquid was pulled through the capillary. However, in our studies, for simplicity, the liquid layer covered the entire cathode surface at the bottom.

Figure 1 also illustrates the use of adaptive Cartesian mesh to resolve the gas-liquid interface. When the liquid surface evolves and plasma is generated in the gas phase, the mesh can be dynamically refined based on the shape of the liquid surface, as well as the electric field, the electron density gradient, or any other quantity that requires high resolution in some parts of a computational domain.

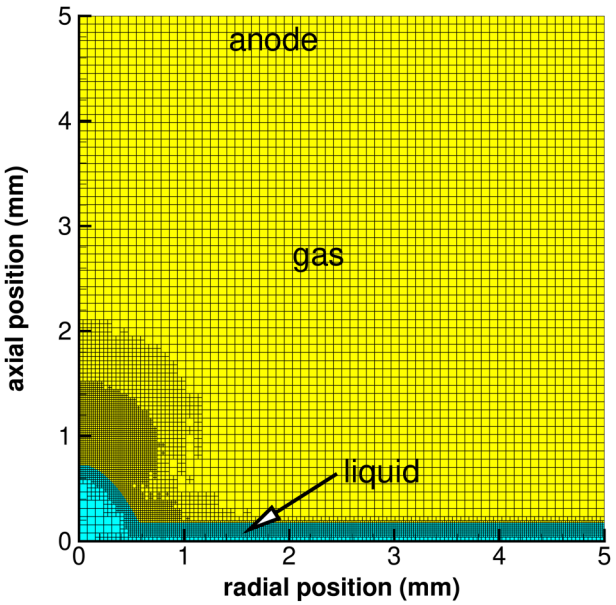

FIG. 1. Two-dimensional axisymmetric simulation domain with adaptive mesh refinement.

The electric field strength in Eq. (3) is calculated by Poisson's equation,

$$\nabla(\varepsilon_0\varepsilon_r\nabla\varphi) = -\rho_e, \tag{4}$$

where ε_0 is the permittivity of free space, ε_r is the gas/liquid electric permittivity, and ρ_e is the charge density. Inside the conductive liquid, we solve the following charge conservation equation:[29]

$$\frac{\partial\rho_e}{\partial t} + \nabla\cdot\boldsymbol{J} = 0, \tag{5}$$

where $\boldsymbol{J} = K\boldsymbol{E} + \rho_e\boldsymbol{u}$ is the current density inside the liquid, $\boldsymbol{E}$ is the electric field, and K is the liquid conductivity. The first term in the definition of $\boldsymbol{J}$ is the ohmic charge conduction, while the second is due to the advection of charges.[29]

The voltages considered in the present studies are insignificant for the liquid heating, bubble formation and their growth, and cavitation.[30] Therefore, the liquid water energy balance is neglected under the conditions of our studies.

The second submodel considers the gaseous plasma dynamics. Since the gap breakdown occurs on the fast (electron) time scale (see discussion in Sec. IV), the liquid evaporation and the heavy particle transport inside the liquid are frozen on the electron time scale. The transport and chemistry processes that occur on the ion/neutral time scale will be studied in future works.

In gas and plasma phases, the space charge is calculated from densities of electrons and ions as $\rho_e = e\left(n_e - \sum_{j=1}^{N} Z_j n_j\right)$, where e is the elementary charge, $n_{j,e}$ are the ion and electron number densities in the gas phase, and Z_j is the ion charge (+1 for positive ions and −1 for negative ions). The sum is taken over all ions considered in the model. The transport of charged particles in the gas phase is modeled using the drift-diffusion approximation that is appropriate for highly collisional plasma of atmospheric-pressure discharges,[31–33]

$$\frac{\partial n_l}{\partial t} + \nabla\cdot\boldsymbol{\Gamma}_l = G_l, \tag{6}$$

where n_l and $\boldsymbol{\Gamma}_l$ are the number density and number flux of lth species, respectively, and G_l is the net rate of their volume production. Equation (6) is solved for both electrons and ions. The transport and chemistry of neutral species are ignored in the present paper. The rates of electron-induced reactions are computed as functions of the mean electron energy using local Boltzmann solver BOLSIG+.[34]

The species flux terms are calculated by

$$\boldsymbol{\Gamma}_l = s_l\mu_l n_l\boldsymbol{E} - D_l\nabla n_l, \tag{7}$$

where μ_l and D_l are the mobility and diffusion coefficient of lth species, and $s_l = +1$ for positive ions, while $s_l = -1$ for electrons and negative ions. The electron transport properties are computed as functions of electron temperature, T_e, while the ion transport properties are taken from available experimental data. The mean electron energy, ε, is defined in terms of the electron temperature as

$$\varepsilon = \frac{3}{2}n_e k_B T_e, \tag{8}$$

where k_B is the Boltzmann constant, and ε is defined by the electron energy conservation equation

$$\frac{\partial\varepsilon}{\partial t} + \nabla\cdot\boldsymbol{\Gamma}_\varepsilon = S_\varepsilon. \tag{9}$$

Here, $\boldsymbol{\Gamma}_\varepsilon$ is the energy flux defined as

$$\boldsymbol{\Gamma}_\varepsilon = \frac{5}{3}\mu_e\boldsymbol{E}\varepsilon - \frac{5}{3}D_e\nabla\varepsilon. \tag{10}$$

The source term S_ε in Eq. (9) is defined as

$$S_\varepsilon = -e\boldsymbol{E}\cdot\boldsymbol{\Gamma}_e - \sum_{j=1}^{N} k_j n_g n_e \Delta\varepsilon_j - \frac{3}{2}k_B n_e \sum_{j=1}^{N_1} n_{g,j}k_{m,j}\frac{2m_e}{m_j}(T_e - T_g). \tag{11}$$

Here, $n_{g,j}$ and T_g are the background gas number densities and temperature, respectively, m_e and m_j, are the electron mass and the mass of the background gas molecules, $\Delta\varepsilon_j$ is the electron energy lost in inelastic collision with neutral, and k_j and $k_{m,j}$ are, respectively, the inelastic collision and momentum transfer rate coefficients. The first term on the right-hand side of Eq. (11) describes the electron ohmic heating, the second term is the contribution of inelastic electron-neutral collisions, and the last term is the contribution of elastic collisions. Both ions and neutrals are assumed to have a common temperature, T_g, which is taken equal to the room temperature (300 K).

Due to the disparity in plasma and liquid time scales, the time step used for the liquid submodel was much longer than that for the plasma submodel. Due to the time-explicit scheme for surface tension, the time step for the liquid model was defined by $\Delta t_{liq} = \sqrt{\frac{(\rho_1+\rho_2)\Delta x^3}{2\pi\sigma}}$, where $\rho_{1,2}$ are the gas and liquid mass densities.[35] For the conditions of our studies, the typical value of Δt_{liq} was $\sim 10^{-6}$ s. In analogy, the time step for the plasma submodel was calculated as $\Delta t_{pl} = 0.8\frac{\Delta x}{|v_e|_{max}}$, where $\boldsymbol{v}_e = \mu_e\boldsymbol{E}$ is the largest value of the electron velocity at the previous time step. The typical value of Δt_{pl} was in the range of 10^{-14}–10^{-12} s. The space step Δx was taken at the highest refinement level. For both submodels, this was 8 ($\Delta x \approx 19.5\,\mu$m). Such refinement level allowed us resolving every space scales of the problem (the gas-liquid interface and the Debye lengths).

III. LIQUID ELECTRODE DYNAMICS

This section presents the results of studies of liquid dynamics in external electric fields. The linear stage of the instability of a leaky dielectric surface in the external electric field[36] can be described using Frenkel's dispersion relation[37] obtained for perfectly conducting liquids,

$$\omega_k^2 = \frac{k}{\rho}\left(\rho g + \sigma k^2 - \frac{\varepsilon_0 E^2}{2}k\right). \tag{12}$$

Here, k is the wave number and g is the gravitational acceleration. For the conditions of our studies (small curvature radius and high electric field), the first term in the brackets is at least one order of magnitude smaller than other terms. Therefore, the gravity force is neglected in our simulations. The liquid surface is stable if $\omega_k^2 > 0$. Otherwise, the waves appear and grow at the surface. One can derive from Eq. (12) that the surface is unstable for $0 < k < \frac{\varepsilon_0 E^2}{2\sigma}$. The dominant mode has the wavenumber $k = \frac{\varepsilon_0 E^2}{3\sigma}$ for which $\omega_k^2 = -\frac{1}{6}\left(\frac{\varepsilon_0 E^2}{3\sigma}\right)^2 \frac{\varepsilon_0 E^2}{\rho}$. One can see from these equations that the higher the electric field the shorter the wavelength of instability. One can also estimate the order of magnitude of the critical electric field necessary for the development of instability. Assuming $k \sim \frac{1}{R}$, where R is the curvature radius of the hump at the liquid surface, one finds

$$E_{cr} \sim \sqrt{\frac{2\sigma}{\varepsilon_0 R}}. \tag{13}$$

The surface tension of water used in our studies is $\sigma = 72 \times 10^{-3}$ N/m. Then, substituting $R \sim 0.5$ mm, one estimates $E_{cr} \sim 6 \times 10^6$ V/m, which gives the correct estimate of the electric field strength necessary for instability of the liquid surface.

The liquid considered in the present paper is water ($\varepsilon_r = 80$), and the background gas is the dry air ($\varepsilon_r = 1$). The liquid conductivity was set to 11.5 mS/cm as in the experiments in Ref. 8. In our simulations presented below, a hemispherical liquid hump having the curvature radius of $R = 0.5$ mm was initially placed at the liquid surface. This was done in analogy to the experiments reported in Ref. 8 in which the capillary forces created such a hump. The initial curvature of the liquid surface allows one to obtain the highest electric field in the known location.

As it follows from Eq. (3), there are two competing forces acting on the liquid surface immersed within the electric field. These are the surface tension force and the electric force. The surface tension tries to smooth out the liquid surface, while the electrostatic force pulls the surface toward the oppositely charged electrode. For the conditions of our studies, the electric force is the dominant if the cathode-anode gap voltage exceeds $\varphi_{cr} \sim 5.5$ kV, which is in rather good agreement with the results reported in Ref. 8. Below this voltage, the liquid surface is smoothed out by the surface tension. Further, we present the results of simulations obtained only for $\varphi_C = -6$ kV. For this value, the electric field E_{cr} [Eq. (13)] is obtained at the protrusion vertex.

Figure 2 shows the time evolution of the liquid surface. One can see that a Taylor cone[11] forms after ~2.0 ms. The cone is formed because the electric field force is greater than the surface tension force. In our simulations, the initial shape of the liquid hump is hemispherical, i.e., the surface tension force is constant along the hump surface. However, the electric field is the largest at the hump head. Therefore, this field pulls the liquid toward the opposite electrode (in this case, anode). The electric field at the cone apex increases with time. On the one hand, this is obtained because the Taylor cone formation results in the decrease of the curvature radius of cone apex. This results in further enhancement of the electric field at the cathode tip. On the other hand, the liquid cathode moves toward the anode during the cone formation. The decrease of the cathode-anode gap leads to the increase of the electric field between the electrodes. Thus, the electrostatic force on the apex increases with time.

The black line in Fig. 2(b) shows the cone angle of ~47°, which is smaller than the value predicted by Taylor's theory (~49.3°).[11] The deviation from this theory was discussed in numerous papers (see, for instance, Ref. 38) and was confirmed experimentally (see Ref. 36 and references therein). As it follows from Fig. 2(c), the cone vertex is unstable. There is no strict balance between the electric field stress and the stress associated with the surface tension, i.e., there is the dynamic Taylor cone formation.[20] As was pointed out in Ref. 20, Taylor's mathematical analysis was carried out for hydrostatic equilibrium. When the liquid moves, there are associated pressure differences, and the situation is not of static equilibrium.

One can see from Fig. 3 the growth of jet from the cone vertex. Once the jet length reaches some critical value, it disintegrates into microdroplets. The jet instability in the external electric field was analyzed in Ref. 21. The authors showed that the droplets with the typical size of ~10 Å are formed due to the Rayleigh instability, while the droplets of larger size (~10 μm) are formed due to the Faraday instability. The latter mechanism was used in deriving Eq. (12) in Ref. 37. Figure 3 also shows that the distance between the droplets is not constant. This is explained by the influence of the ejected droplets on the electric field at the cone tip.

In addition, we analyzed the influence of the liquid viscosity on the liquid electrode dynamics. The results of our simulations have shown that the increase of viscosity leads to slight decrease of the cone angle, while the time of the cone formation increases. Figures 4(c) and 4(d) show the liquid dynamics for two values of the liquid viscosity taken at the same time. One can conclude that the increase of the viscosity prevents the liquid jet formation. Instead, the liquid droplets come off the cone vertex. Also, one can note that

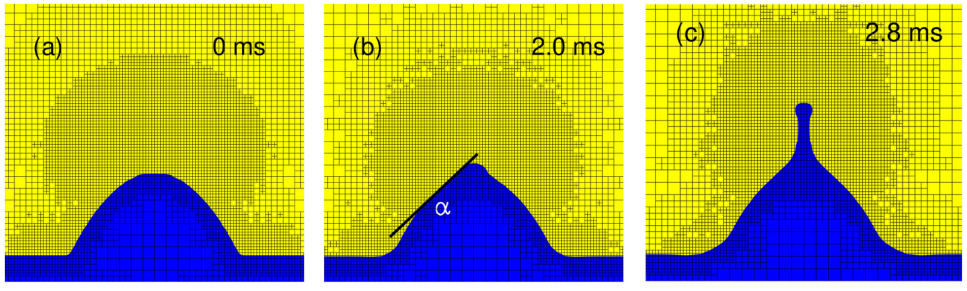

FIG. 2. The surface time evolution: (a) 0 ms, (b) 2.0 ms, and (c) 2.8 ms. Liquid viscosity is $\mu_0 =$ 0.0024 Pa · s.

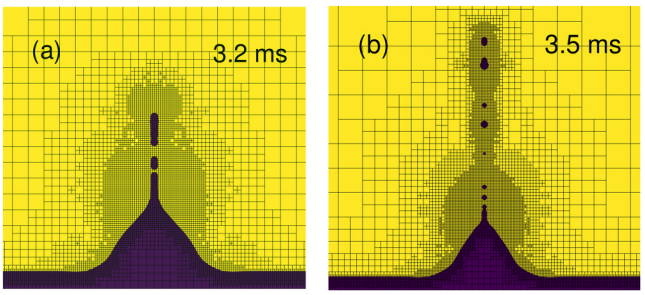

FIG. 3. The surface time evolution: (a) 3.2 ms and (b) 3.5 ms. Liquid viscosity is $\mu_0 = 0.0024$ Pa · s.

the distance between two adjacent droplets increases for increasing viscosity (i.e., the frequency of the droplets ejection decreases).

The increasing liquid viscosity leads to the increase of the role of viscous stress in Eq. (1). As a consequence, at some value of μ, it starts exceeding the surface tension. Therefore, there is the viscous stress rather than the surface tension force that balances the electrical stress. This changes the liquid dynamics.[38]

To conclude this section, we point out that the observed time scale of the liquid dynamics is of the order of milliseconds.

IV. DISCHARGE IGNITION

In this section and Sec. V, the plasma generation over the liquid electrode is analyzed. Since the time scale of the discharge ignition is of the order of a few nanoseconds (electron scale) and the time scale of the liquid motion is of the order of a few milliseconds, the liquid shape is kept frozen during the plasma generation studies. This means the Navier-Stokes equations are switched off.

The simulations were carried out for the atmospheric pressure dry air (78% of nitrogen and 22% of oxygen). Since we are only interested in the physical mechanism of gas breakdown, the simplest set of gas-phase reactions was used. These include the direct ionization of N_2 and O_2 by electron impact, the attachment of electrons to O_2 (generation of negative ions O_2^-), and the electron-ion and ion-ion recombination. More complex plasma chemistry can be included in future studies. In the energy balance of electrons (8), we took into account inelastic processes such as excitation of vibrational and electronic levels of both N_2 and O_2.

The simulation results have shown that the discharge is not ignited for the applied voltage below than −5 kV. This value is in rather good agreement with the experimental results reported in Ref. 8 for similar geometry. We have also obtained that the secondary electron emission due to ion impact from the liquid surface is critical for the discharge ignition. In the present studies, the secondary emission coefficient was set to $\gamma = 0.02$. Note that this value is larger than that discussed in the literature.[9]

Figures 5–9 show the simulation results obtained for the cathode-anode gap voltage of −5 kV. One can distinguish two stages of the discharge development. The first stage is shown in Fig. 5. At this stage, an electron corona is formed in the vicinity of the liquid surface in the region of the highest electric field. The electron density in this corona increases, while it propagates from the cathode to the anode [see Fig. 5(d)]. One can see that it

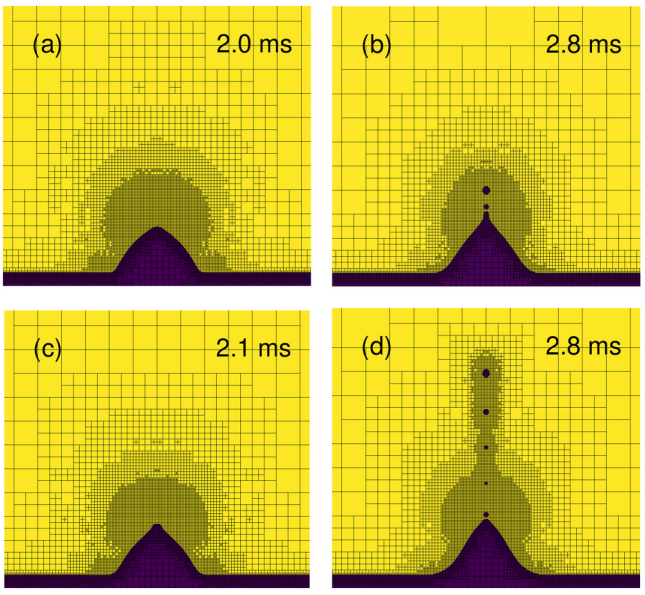

FIG. 4. The surface time evolution for two different liquid viscosities: (a,b) t = 2.0 ms and (b) t = 2.8 ms, viscosity is $\mu = 4\mu_0$; (c,d) $\mu = 16\mu_0$.

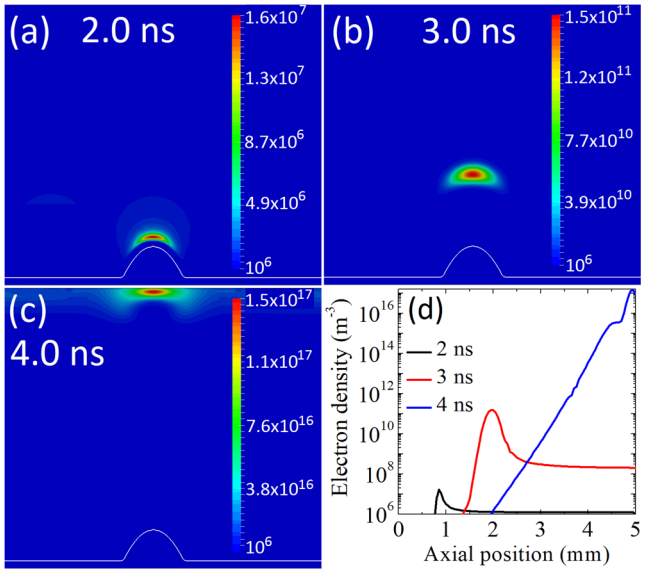

FIG. 5. Electron density (in m^{-3}) obtained at different times: (a) 2.0 ns, (b) 3.0 ns, and (c) 4.0 ns. (d) Axial distribution of the electron density. Applied voltage is −5 kV.

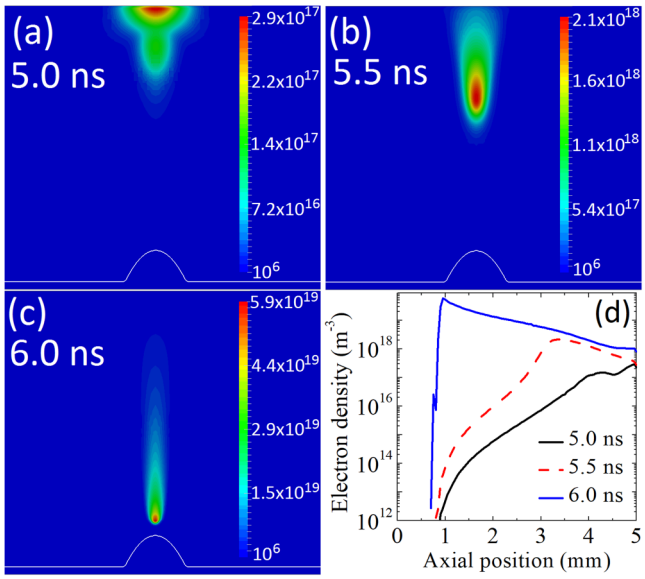

FIG. 6. Electron density (in m^{-3}) obtained at different times: (a) 5.0 ns, (b) 5.5 ns, and (c) 6.0 ns. (d) Axial distribution of the electron density. Applied voltage is −5 kV.

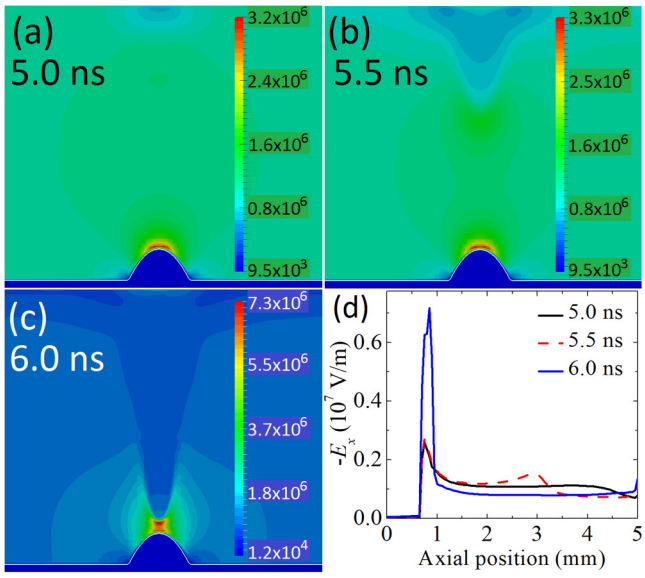

FIG. 8. Electric field (in V/m) obtained at different times: (a) 5.0 ns, (b) 5.5 ns, and (c) 6.0 ns. (d) Axial distribution of the axial component of the electric field. Applied voltage is −5 kV.

reaches $\sim 10^{17}\ m^{-3}$ when it approaches the anode. The corona plasma density is insufficient to disturb the applied electric field. Therefore, no streamers were formed at the considered conditions. The propagating ionization wave leaves behind the tail of positive and negative ions, which can be considered as unmovable at the electron time scale.

Since at the given conditions the electric field is not screened by the plasma, the corona leaves the cathode-anode gap, if one sets $\gamma = 0$. This leads to the discharge extinction. However, if the secondary electron emission is turned on, the second stage of the

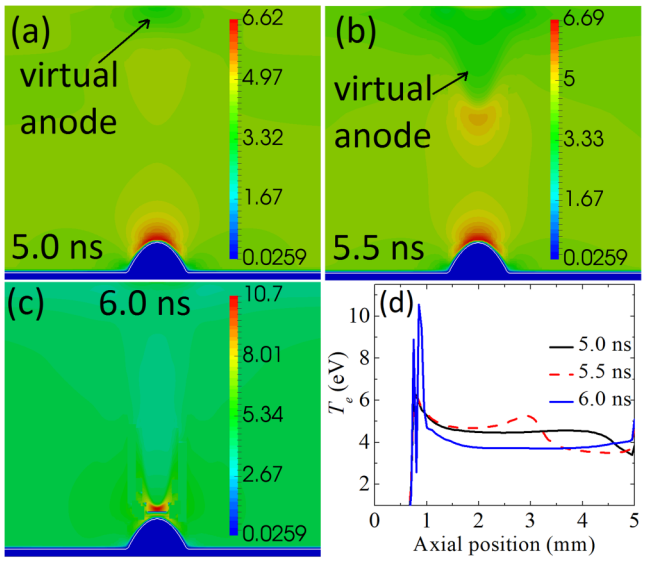

FIG. 7. Electron temperature (in eV) obtained at different times: (a) 5.0 ns, (b) 5.5 ns, and (c) 6.0 ns. (d) Axial distribution of the electron temperature. Applied voltage is −5 kV.

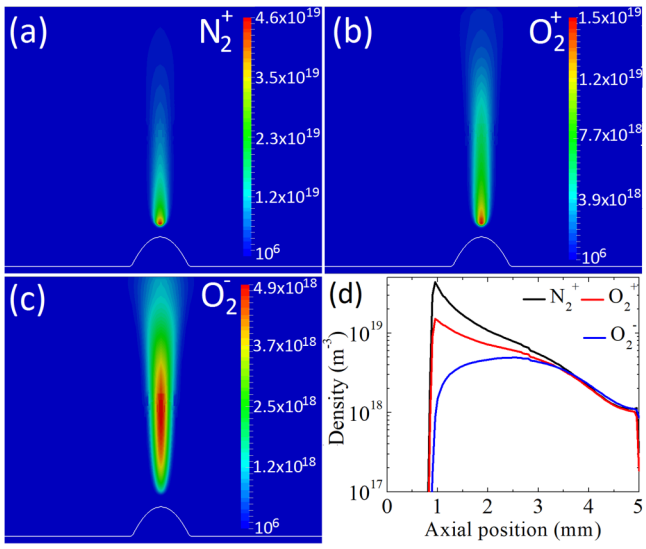

FIG. 9. Density of (a) N_2^+, (b) O_2^+, and (c) O_2^- obtained at t = 6.0 ns. (d) Axial distribution of the ion densities. Applied voltage is −5 kV.

discharge is obtained (see Fig. 6). The comparison between Figs. 5 and 6 shows much shorter time scale of the second stage than the first one. In Ref. 39, this second stage was described as the cathode sheath collapse obtained due to the multiplication of secondary emitted electrons between the cathode and the plasma generated in the vicinity of the anode. This stage looks like the ionization wave propagating from the anode to the cathode [see Fig. 6(d)].

Figure 7 shows the electron temperature, while Fig. 8 shows the electric field distribution during the second stage. One can see that there is a region near the anode, where the electric field is screened by quasineutral plasma. This region can be called a virtual anode because it has the anode potential. The electric field of $\sim 10^5$ V/m penetrates inside this plasma to drive the electron current to the anode. The virtual anode expands toward the cathode due to the multiplication of electrons presented between this anode and the cathode. Under the considered conditions, these are the secondary emitted electrons. Since the virtual anode propagation leads to the decrease of the gap between the electrodes, the electric field in this region increases. This, in turn, leads to the increase of the electron temperature (see Fig. 7) and as a consequence to the increase of the ionization rate coefficient. The latter leads to the nonlinear increase of the ionization wave velocity.

Figure 9 shows the typical densities of positive and negative ions considered in our model. One can see that the densities of positive ions are the largest at the corona's head [see Fig. 9(d)]. This is explained by the highest electron temperature and, as a consequence, the highest ionization rate coefficient there. The negative ion density is the largest in the corona body. Here, the electron temperature decreases because, on the one hand, the electric field is screened by the plasma and does not penetrate in the body. Therefore, the electron ohmic heating is inefficient in this location. On the other hand, electrons experience inelastic collisions with N_2 and O_2 and dissipate their energy in these collisions. The decrease of the electron temperature leads to the increase of the attachment rate coefficient.

V. THE INFLUENCE OF THE LIQUID SURFACE SHAPE AND APPLIED VOLTAGE

This section presents the results of simulations obtained for the applied voltage of −6 kV for two shapes of the cathode protrusion. Figures 10 and 11 show the electron density obtained for the undisturbed protrusion, while Figs. 12 and 13 show the results obtained for the protrusion transformed into the Taylor cone. In both cases, the secondary electron emission coefficient from the liquid surface due to the ion impact was set to 0.02.

One can conclude that both the applied voltage and the shape of the liquid electrode influence the breakdown dynamics. Similar result was recently reported in Ref. 40. Our simulations have shown that the increase of the voltage for the undisturbed protrusion shape results in the faster multiplication of corona electrons. Figure 10 shows that their density reaches the value of $\sim 10^{18}$ m^{-3} when the corona has not reached the anode. This plasma density is sufficient to screen the applied voltage. As a consequence, the second stage of breakdown differs from that obtained for −5 kV (see Sec. IV). Figure 11 shows two ionization waves. The first one

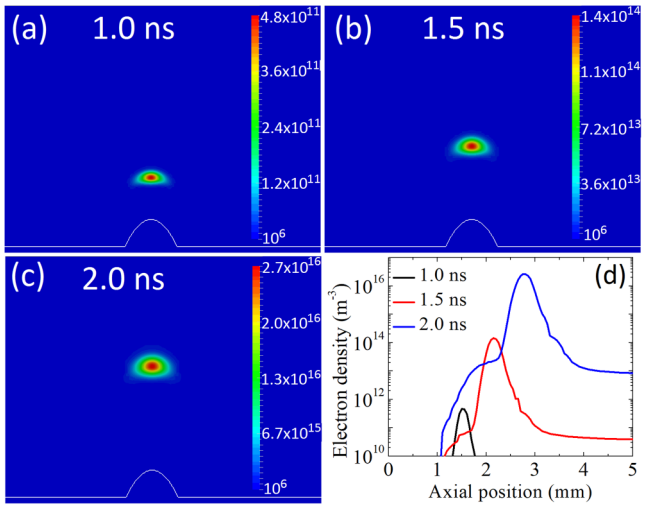

FIG. 10. Electron density (in m^{-3}) obtained at different times: (a) 1.0 ns, (b) 1.5 ns, and (c) 2.0 ns. (d) Axial distribution of the electron density. Applied voltage is −6 kV.

propagates between the dense plasma and the anode, while the second wave propagates between the plasma and the cathode. The former one propagates due to the multiplication of initially seeded electrons (density 10^6 m^{-3}) that are present in the vicinity of the anode. The second ionization wave propagates due to the plasma generation by the secondary electrons.

Figures 12 and 13 show the electron density obtained for the protrusion in the form of a Taylor cone. In this simulation, we first have frozen the plasma and analyzed the evolution of the liquid

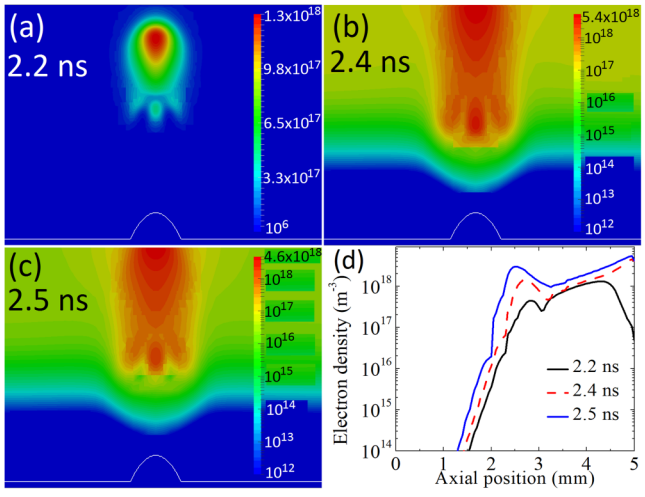

FIG. 11. Electron density (in m^{-3}) obtained at different times: (a) 2.2 ns, (b) 2.4 ns, and (c) 2.5 ns. (d) Axial distribution of the electron density. Applied voltage is −6 kV.

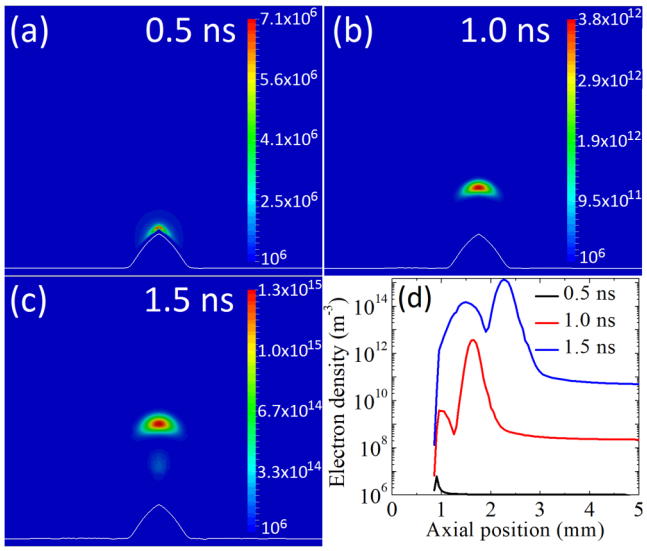

FIG. 12. Electron density (in m^{-3}) obtained at different times: (a) 0.5 ns, (b) 1.0 ns, and (c) 1.5 ns. (d) Axial distribution of the electron density. Applied voltage is −6 kV; the liquid shape is modified by the electric field.

shape in the external electric field. Once the cone was formed, we have frozen the liquid shape and switched on the plasma submodel. As it follows from the discussion in Secs. III and IV, this can be done due to ∼6 orders of magnitude difference in the time scales for liquid and plasma dynamics.

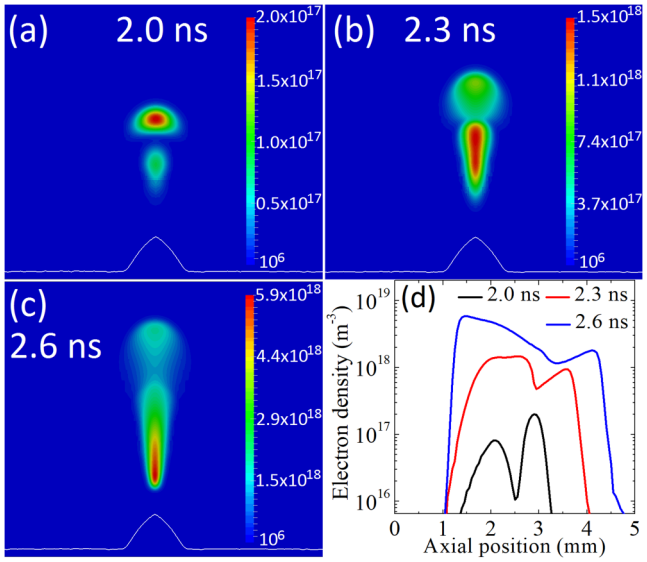

FIG. 13. Electron density (in m^{-3}) obtained at different times: (a) 2.0 ns, (b) 2.3 ns, and (c) 2.6 ns. (d) Axial distribution of the electron density. Applied voltage is −6 kV; the liquid shape is modified by the electric field.

The Taylor cone formation influences the discharge dynamics through the influence on the electric field. Namely, for the given cathode potential, the cone formation increases the electric field. Since the electric current through the liquid is negligibly small, there is no liquid cathode heating, obtained, for instance, in the case of liquid metal electrodes.[41] Therefore, there is no intense evaporation of the electrode material. Also, the electric field at the cone vertex is of the order of 10^7 V/m, which is insufficient for the initiation of electron field emission.[42]

As in the case of the undistorted protrusion (see Fig. 10), the corona density reaches the value of $\sim 10^{18}$ m^{-3} far from the anode [see Fig. 13(a)]. Therefore, there are again two ionization waves at the second stage of discharge. However, now the ionization wave propagating toward the cathode is much faster than the one propagating toward the anode. This is due to much larger electric field between the quasineutral plasma and the cathode.

VI. CONCLUSIONS

A two-dimensional axisymmetric model of atmospheric-pressure discharges in air ignited over a liquid water cathode has been presented. This model takes into account both the liquid electrode motion under the influence of the applied electric field and plasma generation by electron impact and surface emission in the gas phase during the gas breakdown.

First, we have analyzed the influence of the applied voltage on the liquid electrode dynamics. The critical electric field required for the Taylor cone formation at the liquid surface was found. We have also studied the influence of the liquid viscosity on the liquid jet ejection from the Taylor cone vertex. It was obtained that the cone angle is smaller than the one predicted by Taylor's theory. We showed that increasing the liquid viscosity results in the suppression of the jet formation and decreases the frequency of microdroplets ejection. Also, the larger the viscosity the smaller was the cone angle. It was shown that the liquid dynamics occurs at the millisecond time scale.

Second, we have studied the dynamics of gas breakdown over liquid electrodes. We have obtained that gas breakdown occurs at nanosecond time scale and develops into two stages. During the first stage, a fast ionization wave propagates from the liquid hump to the anode. This stage was simulated for different shapes of the hump. Its shape influenced only the corona plasma density and the distance from the anode at which this corona stopped. The second stage was initiated by the secondary electrons emitted from the liquid cathode due to ion impact. We have demonstrated that the second stage develops much faster than the first one, as previously predicted by the theory. During the gas breakdown, which occurs at the electron time scale, the ion motion can be neglected. Indeed, the liquid can also be considered motionless during this fast discharge development time.

To conclude, we have demonstrated that the dynamics of multiphase plasmas containing gas, plasma, and liquid states is characterized by three disparate time scales: the fast electron scale, the slow ion time scale, and the slowest time scale of liquid dynamics. These scales differ by orders of magnitude, and the disparity of the time scales can be used to simplify the description of the system. In the present paper, we have not studied processes that occur at the

ion time scale. These processes can be associated with complex heterogeneous chemical reactions in the gas and liquid phases near the gas-liquid interface. Due to the disparity of the time scales, it is expected that at the ion time scale, the liquid remains motionless, and the electrons are in quasistatic equilibrium with the electric fields. The processes occurring at the ion time scale will be studied in our future work.

ACKNOWLEDGMENTS

This work was supported by the DOE SBIR Project No. DE-SC0015746 and by the NSF EPSCoR Project No. OIA-1655280.

REFERENCES

[1]A. Hickling and M. D. Ingram, J. Electroanal. Chem. **8**, 65 (1964).
[2]S. K. Sengupta and O. P. Singh, J. Electroanal. Chem. **301**, 189 (1991).
[3]P. Gupta, G. Tenhundfeld, E. O. Daigle, and D. Ryabkov, Surf. Coat. Technol. **201**, 8746 (2007).
[4]J. A. Robinson, M. A. Bergougnou, G. S. P. Castle, and I. I. Inculet, IEEE Trans. Ind. Appl. **37**, 735 (2001).
[5]T. Sugimoto, K. Asano, and Y. Higashiyama, J. Electrost. **53**, 25 (2001).
[6]P. Bruggeman, L. Graham, J. Degroote, J. Vierendeels, and C. Leys, J. Phys. D Appl. Phys. **40**, 4779 (2007).
[7]P. Bruggeman, P. Guns, J. Degroote, J. Vierendeels, and C. Leys, Plasma Sources Sci. Technol. **17**, 045014 (2008).
[8]N. Shirai, R. Sekine, S. Uchida, and F. Tochikubo, Jpn. J. Appl. Phys. **53**, 026001 (2014).
[9]P. Bruggeman and C. Leys, J. Phys. D Appl. Phys. **42**, 053001 (2009).
[10]P. J. Bruggeman, M. J. Kushner, B. R. Locke, J. G. E. Gardeniers, W. G. Graham, D. B. Graves, R. C. H. M. Hofman-Caris, D. Maric, J. P. Reid, E. Ceriani, D. Fernandez Rivas, J. E. Foster, S. C. Garrick, Y. Gorbanev, S. Hamaguchi, F. Iza, H. Jablonowski, E. Klimova, J. Kolb, F. Krcma, P. Lukes, Z. Machala, I. Marinov, D. Mariotti, S. Mededovic Thagard, D. Minakata, E. C. Neyts, J. Pawlat, Z. Lj Petrovic, R. Pfleger, S. Reuter, D. C. Schram, S. Schröter, M. Shiraiwa, B. Tarabova, P. A. Tsai, J. R. R. Verlet, T. von Woedtke, K. R. Wilson, K. Yasui, and G. Zvereva, Plasma Source Sci. Technol. **25**, 053002 (2016).
[11]G. Taylor, Proc. R. Soc. A **280**, 383 (1964).
[12]G. Taylor, Proc. R. Soc. London Ser. A **313**, 453 (1969).
[13]J. Eggers and E. Villermaux, Rep. Prog. Phys. **71**, 036601 (2008).
[14]M. R. Morad, A. Rajabi, M. Razavi, and S. R. Pejman Sereshkeh, Sci. Rep. **6**, 38509 (2016).
[15]A. Jaworek, A. M. Gañán-Calvo, and Z. Machala, J. Phys. D Appl. Phys. **52**, 233001 (2019).
[16]J.-U. Park, M. Hardy, S.-J. Kang, K. Barton, K. Adair, D. Mukhopadhyay, C. Y. Lee, M. S. Strano, A. G. Alleyne, J. G. Georgiadis, P. M. Ferreira, and J. A. Rogers, Nat. Mater. **6**, 782 (2007).
[17]B. W. An, K. Kim, M. Kim, S.-Y. Kim, S.-H. Hur, and J.-U. Park, Small **11**, 2263 (2015).
[18]K. Kim, G. Kim, B. R. Lee, S. Ji, S.-Y. Kim, B. W. An, M. H. Song, and J.-U. Park, Nanoscale **7**, 13410 (2015).
[19]K. Patel, A. Mannsberger, A. Suarez, H. Patel, M. Kovalenko, A. A. Fridman, V. Miller, and G. Fridman, Plasma Med. **6**(3–4), 447 (2016).
[20]V. G. Suvorov and E. A. Litvinov, J. Phys. D Appl. Phys. **33**, 1245 (2000).
[21]V. V. Vladimirov, V. E. Badan, and V. N. Gorshkov, Surf. Sci. **266**, 185 (1992).
[22]N. Y. Babaeva and M. J. Kushner, J. Phys. D Appl. Phys. **42**, 132003 (2009).
[23]D. Levko, A. Sharma, and L. L. Raja, J. Phys. D Appl. Phys. **49**, 285205 (2016).
[24]J. Kruszelnicki, A. M. Lietz, and M. J. Kushner, J. Phys. D Appl. Phys. **52**, 355207 (2019).
[25]J. T. Holgate, M. Coppins, and J. E. Allen, New J. Phys. **21**, 063002 (2019).
[26]A free software program for the solution of partial differential equations on adaptive Cartesian meshes; http://basilisk.fr.
[27]H. Wang, Z. Wang, Z. Zhou, Y. Jiang, J. Wang, Y. Geng, and Z. Liu, J. Appl. Phys. **120**, 053303 (2016).
[28]G. D. Weymouth and D. K.-P. Yue, J. Comput. Phys. **229**, 2853 (2010).
[29]J. M. López-Herrera, S. Popinet, and M. A. Herrada, J. Comput. Phys. **230**, 1939 (2011).
[30]M. N. Shneider and M. Pekker, *Liquid Dielectrics in an Inhomogeneous Pulsed Electric Field* (IOP Publishing Ltd, 2016).
[31]A. Luque, V. Ratushnaya, and U. Ebert, J. Phys. D Appl. Phys. **41**, 234005 (2008).
[32]D. Levko and L. L. Raja, Plasma Source Sci. Technol. **26**, 035003 (2017).
[33]B. Bagheri, J. Teunissen, U. Ebert, M. M. Becker, S. Chen, O. Ducasse, O. Eichwald, D. Loffhagen, A. Luque, D. Mihailova, J.-M. Plewa, J. van Dijk, and M. Yousfi, Plasma Source Sci. Technol. **27**, 095002 (2018).
[34]G. J. M. Hagelaar and L. C. Pitchford, Plasma Sources Sci. Technol. **14**, 722 (2005).
[35]S. Popinet, Annu. Rev. Fluid Mech. **50**, 49–75 (2018).
[36]J. F. de la Mora, Annu. Rev. Fluid Mech. **39**, 217 (2007).
[37]Y. I. Frenkel, Phys. Sz. Sowietynion **8**, 675 (1935).
[38]A. L. Yarin, S. Koombhongse, and D. H. Reneker, J. Appl. Phys. **90**, 4836 (2001).
[39]L. D. Tsendin and D. S. Nikandrov, Plasma Source Sci. Technol. **18**, 035007 (2009).
[40]Y. Fu, J. Krek, P. Zhang, and J. P. Verboncoeur, IEEE Trans. Plasma Sci. **47**, 2011 (2019).
[41]E. A. Litvinov, G. A. Mesyats, and D. I. Proskurovskii, Sov. Phys. Usp. **26**, 138 (1983).
[42]D. I. Proskurovsky, IEEE Trans. Plasma Sci. **37**, 1348 (2009).